Defect-Immune Sound Radiation in a Topologically Nontrivial Hyperbolic Metamaterial

Yang Zhang and Li-Yang Zheng*
School of Science, Shenzhen campus of Sun Yat-sen University, 518107 Shenzhen, China

Johan Christensen†
IMDEA Materials Institute, Calle Eric Kandel, 2, Getafe, Madrid 28906, Spain

(Received 30 November 2024; revised 26 February 2025; accepted 27 March 2025; published 18 April 2025)

Topological insulators remain steadfast at the forefront of condensed matter physics due to their unique electronic properties. The well-known bulk-boundary correspondence ensures the existence of robust edge or interface states, which are protected by the topological characteristics of the material's bulk band structure. Moving beyond the bound edge states traditionally emphasized in the literature, we explore how topologically protected states extend to nontrivial radiation away from the confining interfaces. Here, we design a metamaterial whose engineered hyperbolic dispersion entails both chiral and mirror symmetries. We discuss how the associated spin polarization degree of freedom enables defect-immune radiation with a variety of tunable directive far-field patterns. Our experiments unequivocally showcase the topological resilience of acoustic radiation in the wake of willfully added absorptive and obstructive defects, which has the potential to stimulate research into advanced room and urban acoustics.

DOI: 10.1103/PhysRevLett.134.156602

Emission typically refers to the process where energy is released in the form of waves from a source. It encompasses a broad spectrum of wave types and scales. Concerning electromagnetic (EM) waves, light emission spans from the nanometer scale in photon emission [1,2] to the large-scale radiation emitted by celestial bodies [3,4]. Similarly, microwave radiation, characterized by longer wavelengths, exemplifies another facet of EM wave emission, crucial in telecommunications and remote sensing technologies [5]. Beyond EM waves, sound also exhibits emission characteristics when acoustic waves propagate outward from their source, manifesting in infrasound, audible, and ultrasound waves, each with their unique and diverse implications and areas of use [6–8].

In the realm of condensed matter physics, topological insulators have garnered significant attention for their unique electronic properties, particularly the emergence of edge and corner states [9–13]. These states, characterized by their inability to propagate freely and instead being confined to specific points, paths, or boundaries, are at the heart of ongoing theoretical and experimental understanding that expand upon the bulk-edge correspondence. Furthermore, they serve as fundamental building blocks for applications ranging from quantum computing to novel electronic devices [14,15]. The exploration of topological principles extends beyond traditional materials to the community of metamaterials [16–18]. These engineered structures, designed with intricate geometries and periodic arrangements, offer unprecedented control over wave propagation [19,20]. Through methods such as 3D printing and advanced fabrication techniques, a myriad of topological phenomena have been realized, enabling demonstration of robust confined modes analogous to their electronic counterparts, albeit in diverse domains such as optics, acoustics, and mechanics [21,22].

Building upon the principles of symmetry and nontrivial phases inherent in topological insulators, the concept extends naturally to wave emission and radiation. By harnessing these topological attributes, it is desired to bestow emitted waves with enhanced robustness and directional control [23–25], mirroring the confined states observed in electronic systems. This interdisciplinary approach promises transformative advances in manipulating light, sound, and other waveforms for applications in communication, sensing, and beyond. In the context of valley-contrasting physics, advancements in photonic and acoustic research have explored outcoupled valley-edge states, leaked from their confining interfaces [26–29]. These states are localized around specific valleys, characterized by their valley Chern number [30–32], which arises from the breaking of lattice inversion symmetry, facilitating one-way valley transport and precise beam splitting.

In this Letter, we design a hyperbolic metamaterial that, unlike its traditional and topologically trivial forerunners [33,34], provides a hyperbolic dispersion originating from specific symmetries. Chiral symmetry, characterized by the property of objects or molecules that cannot be superimposed onto their mirror image, and mirror symmetry,

*Contact author: zhengly27@mail.sysu.edu.cn
†Contact author: johan.christensen@imdea.org

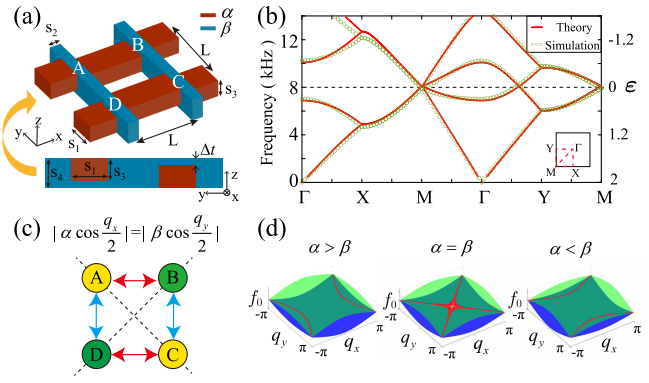

FIG. 1. (a) Two perspectives of a unit cell. The crimson and navy blue tubes represent air channels of different sizes. (b) Dispersion relation from theory (red lines) and simulation (green circles). Nodal features concentrate at $\varepsilon = 0$ ($f_0 \sim 8.1$ kHz). (c) Graphical representation of $\mathcal{H}$. Colored circles represent different chiral nodes. Arrowed lines label the interaction between nodes, and their colors indicate different coupling strengths. Two pseudomirror symmetry lines (dashed lines) appear when $|\alpha \cos q_x/2| = |\beta \cos q_y/2|$. (d) Frequency surfaces of the second and third bands with a hyperbola at f_0 transforming its orientation via a Lifshitz transition at $\alpha = \beta$.

where objects appear identical to their reflections, were both integral to the design, which was tested in a sonic setting at audible frequencies. Accidentally or willfully added imperfections have decremental effects on traditional hyperbolic metamaterials, as impurities or defects seriously hamper the focusing abilities for which these artificial wave-bending materials are known. Here, we experimentally add symmetry-preserving defect absorbers or obstacles (iron pillars) and discuss how the characteristic radiation patterns, which can be individually targeted through a specific spin texture, remain fully intact. We foresee that our findings will stimulate a wealth of research with fundamental and applied implications to wave radiation and steering.

A two-dimensional acoustic metamaterial constructed out of connected narrow waveguide tubes (labeled by crimson and navy blue) is shown in Fig. 1(a), where the unit cell of the lattice contains two elementary air channels (same length $L = 12$ mm). The width and height are $s_1 = 5$ mm, $s_3 = 3$ mm, $s_2 = 2$ mm, and $s_4 = 4$ mm. A staggered offset $\pm\Delta t/2$ in the z direction among crimson channels is introduced to ensure extending a single connecting node ($\Delta t = 0$) to four nodes ($\Delta t \neq 0$), giving rise to sublattices in both the x and y axes. As seen in Fig. 1(a), nodes A and C (B and D as well) are regarded as the same site in the lattice because they have identical neighboring positions. However, nodes A (C) and B (D) are different sublattices that can be considered as chiral pairs. They cannot be mapped onto each other through translation or rotation alone (with respect to the center of the unit cell). This reveals the presence of chiral symmetry where nodes B and D are the chiral partners of nodes A and C. The chiral symmetry enforces the band structure to be symmetric with respect to zero energy since a chiral eigenstate of energy ε always has a chiral partner at $-\varepsilon$. When additional mirror symmetry is imposed, the chiral pair can degenerate at zero energy, forming nodal lines protected by mirror and chiral symmetries. The nontrivial band topology of the nodal lines can be characterized by mirror-winding numbers $(\nu_+, \nu_-) = (1, -1)$; see Refs. [23,35–37]. Further, our cell is designed to have translational symmetries along the two diagonal directions, which effectively induces pseudomirror symmetry for the nodal lines along the same directions. When the couplings along the x, y axes are different, the shape of the pseudomirror lines transform into a nodal hyperbola with nontrivial topology.

Considering only the fundamental waveguide eigenmodes within the channels, wave propagation can be described by a discrete eigenvalue problem [see more in Supplemental Material (SM) [38]], $\mathcal{H}\boldsymbol{\psi} = \varepsilon\boldsymbol{\psi}$ where $\boldsymbol{\psi} = [p_A; p_C; p_B; p_D]$ contains four node pressure amplitudes. The Hamiltonian reads

$$\mathcal{H} = \begin{bmatrix} \mathbf{0} & \boldsymbol{h}^* \\ \boldsymbol{h} & \mathbf{0} \end{bmatrix}, \qquad \boldsymbol{h} = 2\begin{bmatrix} \alpha \cos\frac{q_x}{2} & \beta \cos\frac{q_y}{2} \\ \beta \cos\frac{q_y}{2} & \alpha \cos\frac{q_x}{2} \end{bmatrix}, \quad (1)$$

where $q_{x,y}$ are the normalized wave vectors, and $\alpha = \alpha_0 \sin(kL_x)$, $\beta = \beta_0 \sin(kL_y)$ are the coupling response with $\alpha_0 = 15/23$ and $\beta_0 = 8/23$ the cross sectional ratios [39,40], $k = 2\pi f/c$, with f and c representing frequency and speed of sound, respectively. $L_{x,y}$ represent the effective coupling lengths between adjacent nodes. Under a low-frequency approximation, i.e., $s_1, s_2, s_3, s_4 \ll L$, we have $L_x = L_y = L$. However, due to the finite geometrical sizes of the channels in our implementation, we find $L_x \approx 12$ mm and $L_y \approx 8.2$ mm. The band structure of $\mathcal{H}$ (red lines) consistent with numerical simulations (circles) is shown in Fig. 1(b), verifying a symmetric line with respect to $\varepsilon = 0$ ($f_0 \sim 8.1$ kHz). A double Dirac cone at the M point is formed due to choosing an extended unit cell, which creates band folding. The pseudo mirror planes of $\mathcal{H}$ can be visualized from its matrix graph in Fig. 1(c). Colored circles represent different chiral nodes. Arrowed lines label the interaction between sites, and the line colors indicate different coupling strengths. The graph exhibits two pseudomirror symmetry planes (dashed lines) as long as $|\alpha \cos(q_x/2)| = |\beta \cos(q_y/2)|$, which directly leads to the hyperbolic dispersion at f_0, expressed as

$$\frac{\sin^2\left(\frac{q_x}{2}\right)}{\beta^2} - \frac{\sin^2\left(\frac{q_y}{2}\right)}{\alpha^2} = \frac{\alpha^2 - \beta^2}{\alpha^2\beta^2}. \quad (2)$$

The isofrequency surfaces of the second (blue) and the third (green) bands are depicted in Fig. 1(d), where the crossings of the two surfaces highlighted by red curves form the symmetry-protected nodal lines. As can be seen,

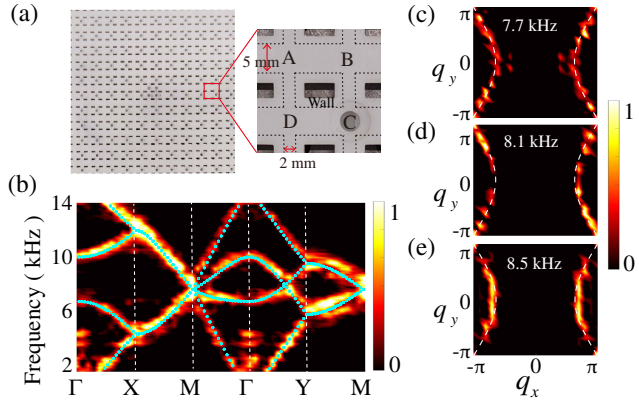

FIG. 2. (a) The hyperbolic metamaterial sample and its unit cell. (b) The measured band structure. Color level indicates the intensity of states. Green dots represent simulation result. (c)–(e) Isofrequency contours at 7.7, 8.1, and 8.5 kHz obtained by Fourier transforming the measured data into momentum $q_x - q_y$ space. The dashed lines mark the hyperbola from theory.

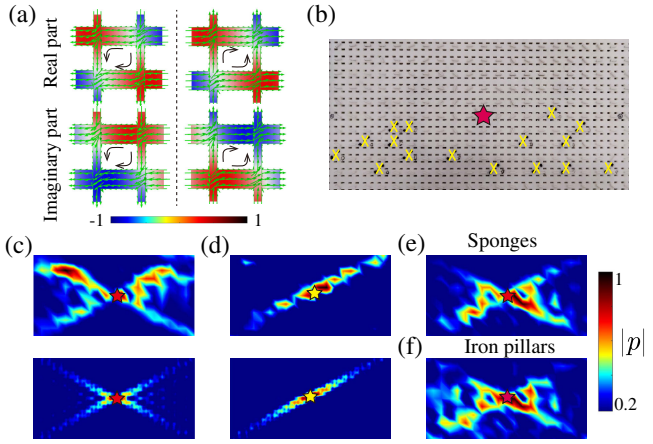

FIG. 3. (a) Two eigenfields at the M point. Arrows indicate the direction of energy flow, and color level represents the amplitude of pressure. (b) The hyperbolic metamaterial with added defects. The red star (yellow crosses) highlights the location of source (defects). (c) Sound emission pattern at 8.2 kHz. Top (bottom) panel corresponds to the measurements (simulations). (d) Bidirectional emission pattern through selective excitation at 8.05 kHz using two point sources at the center (yellow star). Robustness testings of (c) are shown in (e) for absorbing sponges and in (f) for iron pillars at the "×" positions of (b).

the line shape is transformed to different orientated hyperbola with a Lifshitz transition at $\alpha = \beta$ when two lines cross at the Brillouin zone center.

A sample of 21×21 cells fabricated by 3D printing technique is shown in Fig. 2(a) (top view). Each cell features a perforation at node C (enlarged view) that is left open only when the pressure at that node is being recorded. The dashed lines outline the waveguide channels, whose width is 5 mm in the direction of the x axis and 2 mm in that of the y axis. The thickness of the tube wall is 2 mm. To measure the nodal hyperbola, a point source is plugged into the sample center (node C of the center cell) to launch sound propagation into the structure. A function generator is used to sweep a signal ranging from 2–14 kHz, and a microphone is used to probe the sound pressure at each C nodes. By spatially and spectrally collecting the measured data and conducting a Fourier transform, we experimentally obtain the dispersion relation of the structure. The measured band structure (color level indicates the modes intensity) is seen in good agreement with simulations (dots) as depicted in Fig. 2(b). Further, we also verify the existence of the nodal hyperbola predicted by Eq. (2) in the nearest vicinity of the zero energy frequency. The measured isofrequency contours at 7.7, 8.1, and 8.5 kHz are displayed in Figs. 2(c)–2(e). As expected, the three cases indicate a hyperbola following the analytical prediction (dashed curves). This evidence suggests that the hyperbolic topological dispersion is not limited to a single frequency, which enables spectrally broader operation and possibilities for hyperbolic routing and steering.

One appealing property discussed here is the topological resilience to the intrinsic spin Hall texture, which is missing in the conventional scenario with spin polarization degree of freedom only. Because of the pseudomirror and chiral symmetry, $\mathcal{H}$ can be classified into subsystems $\mathcal{H}_\pm \boldsymbol{\psi}_\pm = \varepsilon \boldsymbol{\psi}_\pm$, where $\pm$ is the index denoting the even (+) or odd (−) parity. $\boldsymbol{\psi}_\pm = [\boldsymbol{\psi}_\pm^\uparrow; \boldsymbol{\psi}_\pm^\downarrow] = [p_A \pm p_C; p_B \pm p_D]$ with $\uparrow\downarrow$ denoting the spin polarization index. The subsystem Hamiltonian takes the form

$$\mathcal{H}_\pm = 2\left(\alpha \cos\frac{q_x}{2} \pm \beta \cos\frac{q_y}{2}\right)\boldsymbol{\sigma}_x, \tag{3}$$

where $\boldsymbol{\sigma}_x$ is the Pauli matrix. Equation (3) reveals that sound propagation comprises a linear combination of the $\boldsymbol{\psi}_\pm^{\uparrow\downarrow}$ states. Individually, in Fig. 3(a), we inspect the two eigenstates at the M point from where it is seen they both possess translation symmetry along the diagonal and off-diagonal directions (the pseudomirror symmetry), but the fluxes (green arrows) flow in opposite directions. Thus, engineering flux directions among the states by a proper combination of $\boldsymbol{\psi}_\pm^{\uparrow\downarrow}$ brings forth flexible opportunities for topological radiation of sound.

Topological sound control can be achieved by selective excitations. In Fig. 3(b), we use a point source (8.2 kHz) solely at the highlighted cell (red star, C node) to generate sound propagation in the structure. The measured sound field distribution is obtained in Fig. 3(c) (top panel) by scanning the acoustic pressure at all the C, which displays highly directive emission patterns (color level indicates the pressure strength) comprising bidirectional and symmetrically split radiation. The simulation of the same process is shown in the bottom panel of Fig. 3(c), verifying the sound splitting effect. Furthermore, when using two point sources

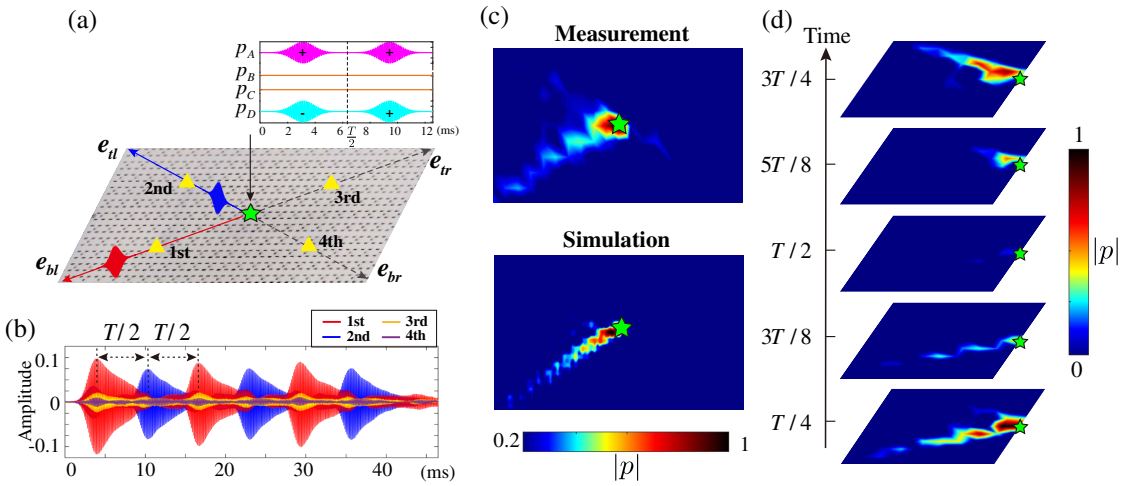

FIG. 4. (a) Directional sound is excited by the modulated signals launched from the center marked by a green star. The yellow triangles are four positions of equivalent distance to the center. Inset shows the modulated signals in a full time period of $T = 12.6$ ms. A pulse propagating along the red (blue) path can be excited in the first (second) half cycle. (b) The pressure amplitudes at the first and second triangle are much stronger than these at the third and fourth triangles. The appearance of the peak at the first and second triangles has a $T/2$ time delay. (c) Unidirectional emission patterns obtained from measurement and simulation. Color level indicates the intensity of pressure. (d) Observation of the switch in direction versus time.

(8.05 kHz) set to be $[p_A, p_C] = [1, 1]$ as excitation (yellow star), we are able to observe a bidirectional sound that propagates from the center to bottom-left (bl) and top-right (tr) corners [Fig. 3(d), top panel]. The corresponding simulation in the bottom panel of Fig. 3(d) also exhibits such a pattern having good agreement with the experiment. The nontrivial topology of the hyperbola is now tested by willfully added imperfections. As long as the mentioned mirror and chiral symmetries are kept, the nodal hyperbola retains topological resilience even when defects appear, adding robustness to the related wave phenomena. In Figs. 3(e) and 3(f), we add symmetry-preserving defects in the form of absorbers and iron pillars, respectively, that are plugged into the B and D nodes of the cells marked by "×." The same excitation as Fig. 3(c) is used to launch sound splitting. The measured pressure field distributions are shown in Fig. 3(e) in the presence of absorbers and in Fig. 3(f) for iron pillars. As seen, both cases largely maintain the splitting radiation patterns without losing the principle signatures.

Another important aspect of the topological hyperbola is that it contains four unidirectional modes that offer unprecedented and flexible possibilities for advanced wave steering. In Fig. 4, we discuss an approach that implies a time varying excitation that targets individual spin Hall textures within the cycle. Within this cycle, different unidirectional modes are targeted, which enables switching the directionality of sound radiation. A cell in the center (green star) is chosen from which sound waves are launched in the structure, and its four node pressure waves are set to be $[p_A, p_C, p_B, p_D,] = [\pm i, 0, 0, 1]$. To achieve this excitation, we experimentally use sinusoidal functions (∼7.9 kHz) with amplitudes of p_A, p_D to be 1 and p_B, p_C to be 0. An additional $\pm\pi/2$ phase difference between p_A and p_D is also imposed. The positive and negative signs can be alternatively obtained by additional time modulations using Gaussian pulses (FWHM = 2.1 ms, periodicity $T = 12.6$ ms, the peaks center at $T/4$ and $3T/4$). The time signals of the four nodes in a full periodicity are depicted in Fig. 4(a). It shows that the modulation amplitudes at p_A and p_D are -1 and $+1$ in the first half cycle, but they are the same $(+1)$ in the second half. Thus, we expect to observe an acoustic pulse propagating along the $\boldsymbol{e}_{\mathrm{bl}}$ direction in the first half cycle, while the pulse appears in the $\boldsymbol{e}_{\mathrm{tl}}$ direction in the second half cycle. The propagations along the $\boldsymbol{e}_{\mathrm{tr}}, \boldsymbol{e}_{\mathrm{br}}$ directions are forbidden. In the measurement, the signal duration of $3T$ is considered, and the acoustic pressure at the four points (yellow triangles, the same distances to the green star) in the four propagating paths are detected. The measured temporal signals are shown in Fig. 4(b), from which we identify clear pulse signals at $t \sim 4.1$, 16.5, 29 ms for the first triangle site and at $t \sim 10.2$, 23, 35.5 ms for the second triangle site. The sound intensities for other sites are very weak during the entire duration. This evidence strongly suggests that the acoustic pulse is routed to propagate along the $\boldsymbol{e}_{\mathrm{bl}}$ direction in the first half cycle, while its direction switches to the $\boldsymbol{e}_{\mathrm{tl}}$ in the second half. In Fig. 4(c), we focus on the radiation pattern for a fixed time $t = 4.1$ ms. The measured sound field distribution shows that sound pressure $(|p|)$ is highly confined solely in the $\boldsymbol{e}_{\mathrm{bl}}$ direction, manifesting the existence of unidirectional sound radiation. The time evolution of acoustic field distribution in a half cycle $(t = [16.5, 23]$ ms) is shown in Fig. 4(d). As expected, the sound emission is seen to be unidirectional and to change direction from the bottom-left (bl) to the top-left (tl) corner.

We have investigated robust radiation by bestowing a hyperbolic metamaterial with strict topology protection by chiral and mirror symmetries. We discussed how leaky acoustic radiation takes on nontrivial and defect-immune attributes, and how the unidirectionally topological states can be individually targeted toward defect-immune radiation. Moreover, we succeeded in controlling two unidirectional modes in time so that the topological radiated wave cyclically alters its focused direction through sequence engineering of different spin textures. We foresee that our findings should stimulate further studies in advanced waves and radiation control.

Acknowledgments—This work is supported by the National Natural Science Foundation of China (Grant No. 12204553) and Fundamental Research Funds for the Central Universities, Sun Yat-sen University (Grant No. 24hytd008).

[1] A. Chynoweth and K. McKay, Photon emission from avalanche breakdown in silicon, Phys. Rev. **102**, 369 (1956).
[2] A. Hayat, P. Ginzburg, and M. Orenstein, Observation of two-photon emission from semiconductors, Nat. Photonics **2**, 238 (2008).
[3] G. A. Dulk, Radio emission from the sun and stars, Annu. Rev. Astron. Astrophys. **23**, 169 (1985).
[4] T. Bastian, A. Benz, and D. Gary, Radio emission from solar flares, Annu. Rev. Astron. Astrophys. **36**, 131 (1998).
[5] D. H. Staelin, Passive remote sensing at microwave wavelengths, Proc. IEEE **57**, 427 (1969).
[6] H. Tian, D. Xie, Y. Yang, T.-L. Ren, Y.-F. Wang, C.-J. Zhou, P.-G. Peng, L.-G. Wang, and L.-T. Liu, Single-layer graphene sound-emitting devices: Experiments and modeling, Nanoscale **4**, 2272 (2012).
[7] H. Shinoda, T. Nakajima, K. Ueno, and N. Koshida, Thermally induced ultrasonic emission from porous silicon, Nature (London) **400**, 853 (1999).
[8] A. Song, J. Li, C. Shen, T. Chen, and S. A. Cummer, Switchable directional sound emission with improved field confinement based on topological insulators, Appl. Phys. Lett. **117**, 043503 (2020).
[9] M. Z. Hasan and C. L. Kane, Colloquium: Topological insulators, Rev. Mod. Phys. **82**, 3045 (2010).
[10] J. G. Analytis, R. D. McDonald, S. C. Riggs, J.-H. Chu, G. Boebinger, and I. R. Fisher, Two-dimensional surface state in the quantum limit of a topological insulator, Nat. Phys. **6**, 960 (2010).
[11] Y. Xu, I. Miotkowski, C. Liu, J. Tian, H. Nam, N. Alidoust, J. Hu, C.-K. Shih, M. Z. Hasan, and Y. P. Chen, Observation of topological surface state quantum Hall effect in an intrinsic three-dimensional topological insulator, Nat. Phys. **10**, 956 (2014).
[12] B.-Y. Xie, H.-F. Wang, H.-X. Wang, X.-Y. Zhu, J.-H. Jiang, M.-H. Lu, and Y.-F. Chen, Second-order photonic topological insulator with Corner states, Phys. Rev. B **98**, 205147 (2018).
[13] C.-W. Chen, R. Chaunsali, J. Christensen, G. Theocharis, and J. Yang, Corner states in a second-order mechanical topological insulator, Commun. Mater. **2**, 62 (2021).
[14] V. Lahtinen and J. Pachos, A short introduction to topological quantum computation, SciPost Phys. **3**, 021 (2017).
[15] S. D. Sarma, M. Freedman, and C. Nayak, Majorana zero modes and topological quantum computation, npj Quantum Inf. **1**, 15001 (2015).
[16] L. Xin, Y. Siyuan, L. Harry, L. Minghui, and C. Yanfeng, Topological mechanical metamaterials: A brief review, Curr. Opin. Solid State Mater. Sci. **24**, 100853 (2020).
[17] F. Zangeneh-Nejad and R. Fleury, Disorder-induced signal filtering with topological metamaterials, Adv. Mater. **32**, 2001034 (2020).
[18] F. Allein, A. Anastasiadis, R. Chaunsali, I. Frankel, N. Boechler, F. K. Diakonos, and G. Theocharis, Strain topological metamaterials and revealing hidden topology in higher-order coordinates, Nat. Commun. **14**, 6633 (2023).
[19] W. Gao, M. Lawrence, B. Yang, F. Liu, F. Fang, B. Béri, J. Li, and S. Zhang, Topological photonic phase in chiral hyperbolic metamaterials, Phys. Rev. Lett. **114**, 037402 (2015).
[20] S. H. Mousavi, A. B. Khanikaev, and Z. Wang, Topologically protected elastic waves in phononic metamaterials, Nat. Commun. **6**, 8682 (2015).
[21] Y. Zhang, B. Li, Q. Zheng, G. M. Genin, and C. Chen, Programmable and robust static topological solitons in mechanical metamaterials, Nat. Commun. **10**, 5605 (2019).
[22] A. Ni and Z. Shi, Robust elastic wave transport in zone-folding induced topological hierarchical metamaterials, Int. J. Mech. Sci. **251**, 108336 (2023).
[23] J.-P. Zheng, L.-Y. Zheng, S.-Y. Yu, S.-L. Yang, X.-C. Sun, L. Liu, M.-H. Lu, Y.-F. Chen, and J. Christensen, Focusing micromechanical polaritons in topologically nontrivial hyperbolic metasurfaces, Adv. Mater. **36**, 2311599 (2024).
[24] C. C. Wanjura, M. Brunelli, and A. Nunnenkamp, Correspondence between non-Hermitian topology and directional amplification in the presence of disorder, Phys. Rev. Lett. **127**, 213601 (2021).
[25] L.-Y. Zheng and J. Christensen, Topological radiation engineering in hyperbolic sonic semimetals, Phys. Rev. B **103**, 064307 (2021).
[26] X. Zhang, L. Liu, M.-H. Lu, and Y.-F. Chen, Valley-selective topological corner states in sonic crystals, Phys. Rev. Lett. **126**, 156401 (2021).
[27] Y. Kang, X. Ni, X. Cheng, A. B. Khanikaev, and A. Z. Genack, Pseudo-spin–valley coupled edge states in a photonic topological insulator, Nat. Commun. **9**, 3029 (2018).
[28] Z.-M. Yu, S. Guan, X.-L. Sheng, W. Gao, and S. A. Yang, Valley-layer coupling: A new design principle for valleytronics, Phys. Rev. Lett. **124**, 037701 (2020).
[29] B.-b. Wang, D. Jia, Y. Ge, S.-q. Yuan, and H.-x. Sun, Acoustic suppressed topological refraction in valley sonic crystals, New J. Phys. **24**, 113033 (2022).
[30] F. Zhang, A. H. MacDonald, and E. J. Mele, Valley Chern numbers and boundary modes in gapped bilayer graphene, Proc. Natl. Acad. Sci. U.S.A. **110**, 10546 (2013).

[31] M. Ezawa, Topological Kirchhoff law and bulk-edge correspondence for valley Chern and spin-valley Chern numbers, Phys. Rev. B **88**, 161406(R) (2013).

[32] H. Pan, Z. Li, C.-C. Liu, G. Zhu, Z. Qiao, and Y. Yao, Valley-polarized quantum anomalous Hall effect in silicene, Phys. Rev. Lett. **112**, 106802 (2014).

[33] C. Shen, Y. Xie, N. Sui, W. Wang, S. A. Cummer, and Y. Jing, Broadband acoustic hyperbolic metamaterial, Phys. Rev. Lett. **115**, 254301 (2015).

[34] S. Dai, Q. Ma, M. Liu, T. Andersen, Z. Fei, M. Goldflam, M. Wagner, K. Watanabe, T. Taniguchi, M. Thiemens, F. Keilmann, G. C. A. M. Janssen, S.-E. Zhu, P. Jarillo-Herrero, M. M. Fogler, and D. N. Basov, Graphene on hexagonal boron nitride as a tunable hyperbolic metamaterial, Nat. Nanotechnol. **10**, 682 (2015).

[35] L. Lu, Z. Wang, D. Ye, L. Ran, L. Fu, J. D. Joannopoulos, and M. Soljačić, Experimental observation of Weyl points, Science **349**, 622 (2015).

[36] W. Deng, J. Lu, F. Li, X. Huang, M. Yan, J. Ma, and Z. Liu, Nodal rings and drumhead surface states in phononic crystals, Nat. Commun. **10**, 1769 (2019).

[37] R. Bi, Z. Yan, L. Lu, and Z. Wang, Nodal-knot semimetals, Phys. Rev. B **96**, 201305(R) (2017).

[38] See Supplemental Material at http://link.aps.org/supplemental/10.1103/PhysRevLett.134.156602 for detailed descriptions of the model and experimental methods.

[39] L.-Y. Zheng, V. Achilleos, O. Richoux, G. Theocharis, and V. Pagneux, Observation of edge waves in a two-dimensional Su-Schrieffer-Heeger acoustic network, Phys. Rev. Appl. **12**, 034014 (2019).

[40] L.-Y. Zheng, V. Achilleos, Z.-G. Chen, O. Richoux, G. Theocharis, Y. Wu, J. Mei, S. Felix, V. Tournat, and V. Pagneux, Acoustic graphene network loaded with Helmholtz resonators: A first-principle modeling, Dirac cones, edge and interface waves, New J. Phys. **22**, 013029 (2020).